Applied Physics A (2019) 125:472
https://doi.org/10.1007/s00339-019-2768-5

Applied Physics A
Materials Science & Processing

Influence of Cr^{3+} substitution on structural, morphological, optical, and magnetic properties of nickel ferrite thin films

Apparao R. Chavan[1] · Mahendra V. Shisode[1] · Pallavi G. Undre[1] · K. M. Jadhav[1]

Received: 6 April 2019 / Accepted: 18 June 2019

Abstract
The $NiFe_{2-x}Cr_xO_4$ ($0.0 \le x \le 1.0$ in the step of $x = 0.2$) thin films have been synthesized using chemical spray deposition technique. The effects of Cr^{3+} content on the structural, morphological, optical and magnetic properties of these thin films have been investigated. The X-ray diffraction patterns confirmed single phase cubic spinel structure with space group of Fd-3m. The lattice constant decreases with increases Cr^{3+} concentration obeying Vegard's law. The functional studied of Cr^{3+} substitution $NiFe_2O_4$ thin films were formed two major transmission bands, high-frequency band (ν_1) around at 665 cm^{-1} is due to intrinsic vibrations of (A) site and the low frequency band (ν_2) around 428 cm^{-1} is due to [B] site, respectively. Surface morphology was investigated in terms of root mean square roughness, average roughness (R_a), surface kurtosis and surface skewness of Ni–Cr ferrite thin films. The energy band gap for allowed direct electronic transition found to be in the range of 2.75–3.02 eV with Cr^{3+} content. According to VSM results show that, the saturation magnetizations of the thin film samples were found to be in the range of 234.12–46.65 emu/cc. The Cr^{3+} concentration increases with a reduction in hysteresis losses as well as slight reduction in the saturation magnetization.

1 Introduction

The spinel ferrites are interesting materials for both fundamental and applied research. They have generated considerable interest among researchers and scientists all across the world due to their versatile properties and applications [1–7]. The spinel ferrites have been intensively advances due to their intrinsic properties and usually tailored by changing compositions for suitable substitutions or unique combination of desirable properties [8]. They have potential applications such as electrical components, transformer core, electronic microwave, ferrofluid technology, biomedical drug delivery, computer memory chip and magnetic recording media [9–12]. The spinel ferrites have higher resistivity of a great interest for large permeability at high-frequency for inductive components. In the past few years, the semiconducting diluted magnetic materials have attracted considerable attention which is due to their promising application for the spintronic devices [13].

Nickel ferrite ($NiFe_2O_4$) is a soft magnetic material having high saturation, low coercivity and high electrical resistivity which are suitable for the magneto-optical and magnetic applications. Also, it has low eddy current loss, excellent catalytic behavior and chemical stability. The $NiFe_2O_4$ is ferrimagnetic in nature for their existing antiparallel spins between Fe^{3+} occupying (A) site and Ni^{2+} occupying [B] site. It is represented by the chemical formula $(Fe^{3+})_A [Ni^{2+}Fe^{3+}]_B O_4^{2-}$ [14, 15]. Generally, $NiFe_2O_4$ is used for the transformer cores, microwave devices and inductors. To adapt the magneto mechanical properties Cr^{3+} substitution in nickel ferrite is preferred. The properties of spinel ferrites effectively depend on chemical compositions, micro structure and synthesis technique [16]. According to literature survey, Singh et al. [17] have prepared Cr^{3+} substitution nickel ferrite thin films and studied physicochemical and electro catalytic properties. The Cr^{3+} ion substitution from 0.2 to 1.0 mol in the nickel ferrite shows the basic oxide electro catalytic-activity increases. For the reaction in 1 M KOH at 25 °C and electro catalytic-activity of the oxide 0.8–1.0 mol Cr^{3+} significantly reported. They observed that values of electro catalytic-activity found to be greater than earlier reports for 0.8 and 1.0 M. The transition metals cations are incorporated in the chromium lattice indicate subsequent changes in their structural, electrical, optical

✉ Apparao R. Chavan
2020chavan@gmail.com

K. M. Jadhav
drjadhavkm@gmail.com

[1] Department of Physics, Dr. Babasaheb Ambedkar Marathwada University, Aurangabad, M. S. 431004, India

Published online: 20 June 2019

and magnetic properties. It depends on the preparation technique, annealing temperature, pH value, microstructure as well as the grain boundaries [18]. Several investigators have investigated the electrical and magnetic properties for Cr^{3+} substitution in the ferrite materials. Lin et al. [19] have prepared Cr^{3+} substituted nickel ferrite using sol–gel auto-combustion technique. The Mossbauer spectra revealed a pair of normal Zeeman split sextets which confirm ferrimagnetic behavior which is due to decreases in magnetic hyperfine field at the tetrahedral site (A) with increasing Cr^{3+} concentration from 0.0 to 1.0. Further the decrease in Ms is observed whereas coercivity varies randomly. The conductivity decreases with increases Cr^{3+} concentration in the nickel ferrite has been reported [20]. Panwar et al. [21] have studied the structural, magnetic and electric properties of $Ni_{1-x}Cr_xFe_2O_4$ ($0.02 \leq x \leq 0.05$) thin film prepared using PLD technique. The structures of prepared thin films are confirmed to be cubic with higher grain size for Si (111) than Si (100) substrate. The observed modifications in magnetic properties are due to occupancy of Ni^{2+} and Fe^{3+} ions at both tetrahedral and octahedral sites. The lattice distortion and strain produced affected the Ms value to decrease rapidly with Cr^{3+} content. In our recent studies, the effect of Cr^{3+} substitution in Co–Cd ferrites nanoparticle has been reported [22]. It was observed that, the saturation magnetization decreases with increase in Cr^{3+} content which is due to lower magnetic moment of Cr^{3+} as compared to Fe^{3+} ions. Furthermore the DC resistivity increases with increase in Cr^{3+} ions. This may be attributed due to the existence of Cr^{3+} ions in only one stable oxidation state so that resistivity of the thin film increases for Fe^{2+} and Fe^{3+} ions.

Nowadays, thin films can be prepared by various techniques in the laboratory. The most versatile films can be prepared by chemical spray deposition technique for the various applications such as solid oxide, fuel cells sensors, solar cells, etc. [23, 24]. The properties of thin film are affected by various parameters such as substrate temperature, droplet size, carrier gas, spray rate, and cooling rate after deposition. Other parameters such as the solution concentration, substrate temperature, quantity of spray solution and distance between spray nozzles to substrate affects thin film parameters [25]. Among them substrate to nozzle distance highly affects the thickness of the thin film. The main advantages of chemical spray deposition technique is larger area of thin films for the simple substituting, easily coating to number of layers, low energy and by changing the parameters thickness of films can be controlled [26–30]. Although there are some reports on the Cr^{3+} substituted nickel ferrite thin films, but to the best of our knowledge, no reports are available in the literature on the spray pyrolysis deposited Cr^{3+} substituted nickel ferrite thin films.

In the present work, the Cr^{3+} substituted $NiFe_2O_4$ thin films were prepared using chemical spray deposition method. The changes in physical properties of pure and substituted samples were studied. The optical and magnetic properties show significant changes with Cr^{3+} substitution. We have investigated structural, microstructural, optical and magnetic properties of Cr^{3+} substituted nickel ferrite thin films.

2 Experimental work

The Cr^{3+} substitutions in nickel ferrite films were deposited on to glass substrate using chemical spray deposition technique. The glass substrates are dipped in chromic acid (0.1 M) for 2 h. After glass substrates are washed in ultra sonication with distilled water. The initial ingredients nitrates of nickel ($Ni(NO_3)_2 \cdot 6H_2O$), ferric ($Fe(NO_3)_3 \cdot 9H_2O$) and chromium ($Cr(NO_3)_3 \cdot 9H_2O$) were used as sources of starting chemicals for Ni^{2+}, Cr^{3+} and Fe^{3+} ions, respectively. The spray solution was mixed in double distilled water with 0.08 M for Ni^{2+}, Cr^{3+} and Fe^{3+} ions. Initially glass substrates were kept at deposition temperature of 380 °C (± 10 °C) with interval of 30 °C for the deposition process and then the solution was sprayed for the deposition. The experimental parameters were well settled before solution was deposited such as the nozzle to substrate distance was kept at 28.5 cm and the spray rate at 3 ml/min. To atomize the spray the gas of compressor was used as a gas carrier. Lastly for formation of crystallinity, the thin films were annealed at 550 °C for 3 h in standard muffle furnace.

The classifications of crystalline phase, lattice constant as well as strain of the films were investigated using X-ray diffraction (BRUKER D8 Advance). The equipment used for FTIR analysis is Perkin-Elmer infrared spectrometer with the model no 78. Surface morphology was achieved by applying the FE-SEM set up (BRUCKER S-4800, Japan). The optical absorption for present films was measured using Perkin-Elmer Lambda in the range of 300–1100 nm. The magnetic properties measured using set up Lakeshore VSM 7410 at room temperature.

3 Results and discussion

3.1 Structural and microstructural studies

The structural investigation of Cr^{3+} substituted nickel ferrite thin films were analyzed by X-ray diffraction as shown in Fig. 1. The X-ray diffraction peaks corresponding to the plane (111), (220), (311), (222), (400), (422), (511), (440) and (533) which confirms cubic spinel structure with space group of Fd-3m. It can be seen from the diffraction peaks, the obtained films are quite similar to the result to Sathyaseelam et al. [31].

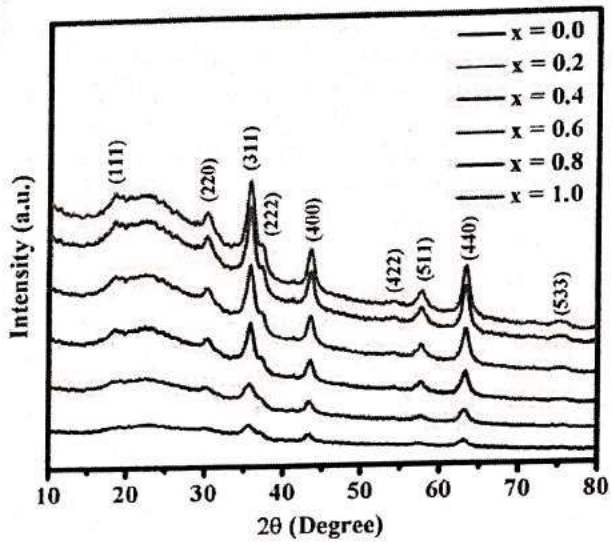

Fig. 1 X-ray diffraction patterns of Cr^{3+} substitution in $NiFe_2O_4$ ($0.0 \le x \le 1.0$, $x = 2$ step)

The crystallite size calculated using Debye–Scherrer's equation [32] and micro-strain using Williamson–Hall plots.

$$D_{XRD} = \frac{0.9\lambda}{\beta \cos\theta}, \tag{1}$$

where λ is the X-ray wavelength, 0.9 is the symmetry constant, θ is the angle of Bragg diffraction and β is the FWHM of the most intensive peak, in degrees. The average crystallite size is obtained 10–24 nm and tabulated in Table 1. The average crystallite size slightly increases with increase in Cr^{3+} ions content. Similar results are reported by Jadoun et al. [33]. As the Cr^{3+} substitution increases the crystallinity rises with the enlargement in peaks and predicts the increase in crystallite size [34]. The average crystallite sizes calculated by Debye–Scherrer's formula and W–H plot are presented in Table 1. The micro-strain of the thin films was calculated using the W–H plot relation [35].

$$\beta \cos\theta = (k\lambda/D) + 4\varepsilon \sin\theta, \tag{2}$$

where D is the crystallite size, k is the Debye–Scherrer constant, and ε is the micro-strain. The strains of the films were estimated using Williamson–Hall plots as shown in Fig. 2. The Williamson–Hall plots of $x = 0.4$ and $x = 0.6$ shows negative slope and compressive strain in the films. The lattice parameters were estimated using following relation [36].

$$a^2 = \frac{\lambda^2 (h^2 + k^2 + l^2)^{1/2}}{4 \sin^2\theta} \tag{3}$$

The lattice constants are obtained from 8.335 to 8.277 Å in the present thin films. The lattice constant decreases with increasing Cr^{3+} concentration (x) which is due to the ionic radii of Cr^{3+} replaced by Fe^{3+}, the similar results are reported by Lakshmi [37]. The X-ray density (ρ_x) have been estimated from the volume of the unit cell and molecular weight of each composition using following equation for the thin films [38].

$$d_x = \frac{nM}{N_A a^3}, \tag{4}$$

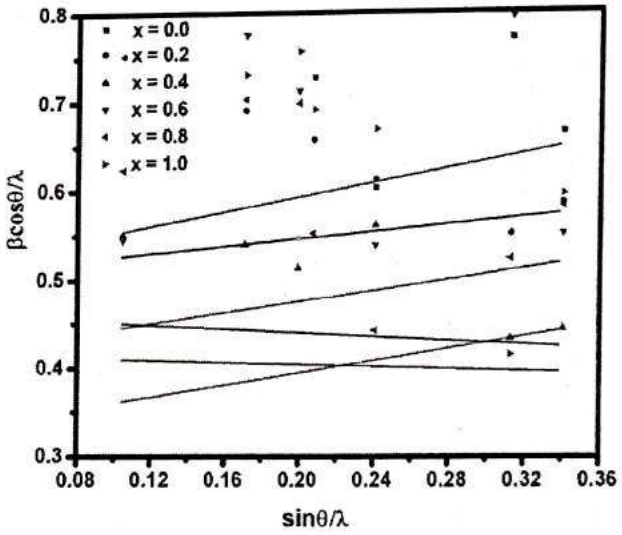

Fig. 2 Williamson–Hall plots ($(\beta \cos\theta)/\lambda$ versus $(\sin\theta)/\lambda$) for the $Ni_{1-x}Cu_xFe_2O_4$ ($0.0 \le x \le 1.0$)

Table 1 Lattice constant (a), X-ray density (d_x) and crystallite size (D) and strain ε (W–H) of $NiFe_{2-x}Cr_xO_4$ ($0.0 \le x \le 1.0$) thin films

Composition X	a (Å) (±0.10)	d_x (g/cm)^3 (±0.01)	D (nm) (±2.0)	ε (W–H) (±0.010)	D (W–H) (nm) (±2.0)
0.0	8.335	5.377	10	0.0507	25
0.2	8.324	4.094	13	0.1013	28
0.4	8.314	4.091	17	−0.0272	31
0.6	8.302	4.091	22	−0.0145	34
0.8	8.287	4.095	19	0.1031	35
1.0	8.277	4.091	24	0.0851	44

where M is the molecular weight of the each composition, N_A is the Avogadro's number, and a is lattice constant for respective films. The decrease in X-ray density (ρ_x) with increase in Cr^{3+} concentration is due to the lower atomic mass of Cr^{3+} as compared to Fe^{3+} [39].

FTIR spectra of Cr^{3+} substituted nickel ferrite thin films in the wavenumber range of 400–4000 cm^{-1} at room temperature against transmittance were recorded. Figure 3 shows that, the lower wave number band represents the trivalent metal oxygen at octahedral [B] sites and the vibration of Fe^{3+}–O^{2-} in the sublattice at tetrahedral (A) site is due to the higher wave number band [40]. In the present thin films, the FTIR spectra exhibiting a strong absorption band (ν_1) around 442 cm^{-1} attributed to Fe–O stretching vibration for unit cell in the tetrahedral (A) site. Other band observed metal–oxygen vibrations in the octahedral [B] site around (ν_2) at 655 cm^{-1} is due to the slight oxidation of the thin films surfaces [41]. The highly sensitivity of the absorption bands changes interaction between cations and oxygen in the films. The Fe^{3+} ions are replaced with the Cr^{3+} ions at octahedral sites so that the shift in absorption band (ν_2) is observed. It is due to lower atomic mass and smaller ionic radius of Cr^{3+} ions. The band at 447 to 457 cm^{-1} is slightly shifted for Cr^{3+} substitution which due to stretching vibration of the Cr–O contribution. The peak at 1519 cm^{-1} is the demonstration of the vibration of Fe–O as shown in Fig. 3. The observed bands at 3556 and 1630 cm^{-1} are attributed to the stretching vibration between H–O–H ions interpreting the presence of free water [42, 43]. These are due to presence of –OH chains that retained during the preparation of spray pyrolysis technique.

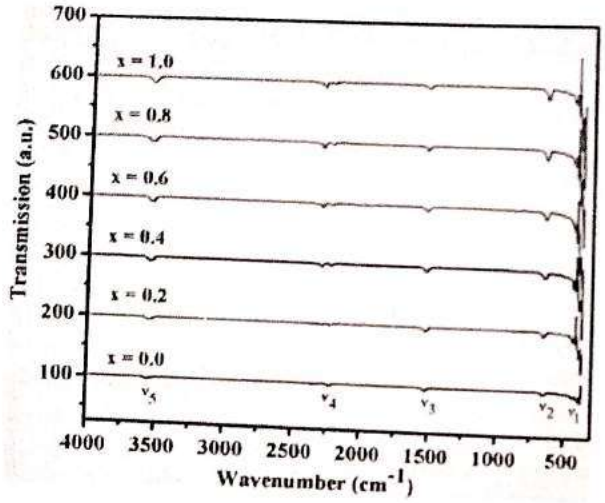

Fig. 3 FTIR spectra of Cr^{3+} substitution in $NiFe_2O_4$ ($0.0 \le x \le 1.0$, $x=2$ step)

From Fig. 4a–d the AFM image shows that, the valley like structure of the surface and hills with the agglomerated grains. AFM images reveal a dense film with well crystallinity that is formed having the spherical grains and films grown on glass surface [44]. All the roughness parameters are tabulated in Table 2. During scanning of AFM images,

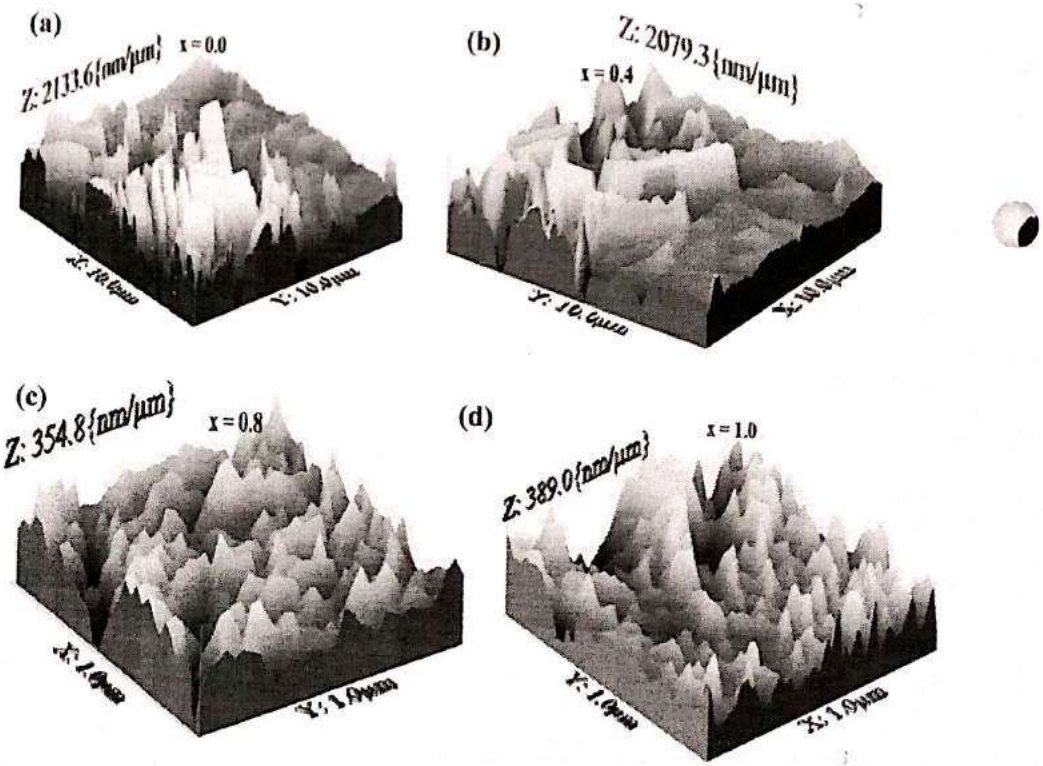

Fig. 4 3-D images AFM of Cr^{3+} substitution in $NiFe_2O_4$ ($0.0 \le x \le 1.0$, $x=2$ step)

Table 2 Average roughness (R_a), root mean square roughness (R_{rms}), skewness (S_{ku}) and Kurtosis (R_{ku}) for AFM, and energy band gap (E_g) for UV–visible and thickness (T) for the $NiFe_{2-x}Cr_xO_4$ ($0.0 \le x \le 1.0$) thin films

x	R_a (μm) (±0.01)	R_{rms} (μm) (±0.01)	R_{sk} (±0.01)	R_{ku} (±0.01)	T (nm) (± 10)	E_g (eV) (±0.01)
0.0	30.83	39.08	0.050	2.865	277	2.98
0.2	–	–	–	–	265	2.83
0.4	36.15	43.14	−0.426	2.561	256	2.79
0.6	–	–	–	–	206	2.60
0.8	60.10	46.59	−0.331	3.066	283	2.45
1.0	39.20	29.18	−0.086	3.877	238	2.37

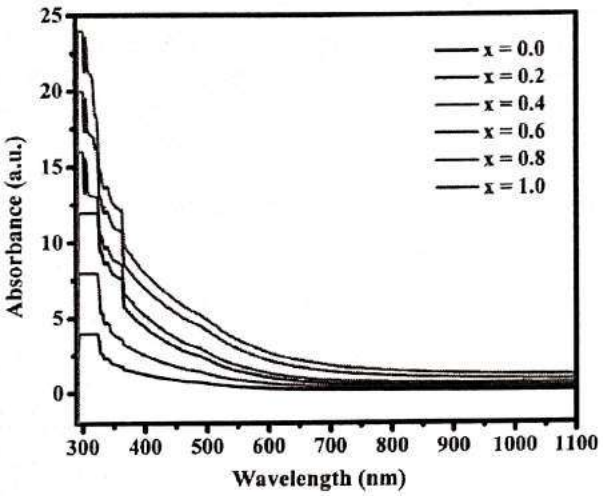

Fig. 5 UV–visible absorbance spectra of $NiFe_{2-x}Cr_xO_4$ ($0.0 \le x \le 1.0$) thin films

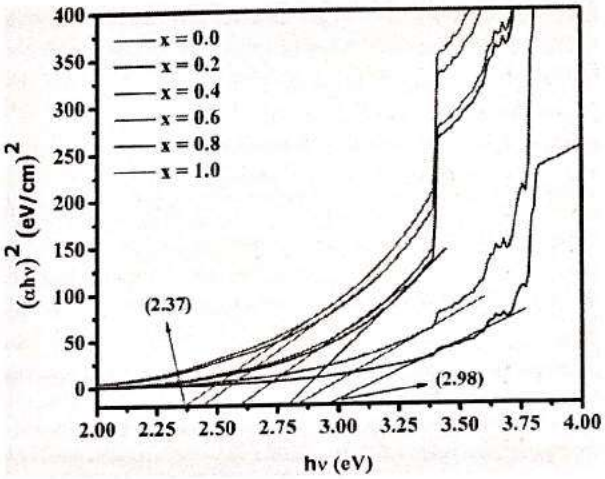

Fig. 6 Variation of $(\alpha h\nu)^2$ with photon energy ($h\nu$) of Cr^{3+} substitution in $NiFe_2O_4$ ($0.0 \le x \le 1.0$, $x=2$ step)

the fine droplets predict the good quality growth of Cr^{3+} substitution.

3.2 Optical properties

The optical measurements of Cr^{3+} substituted $NiFe_2O_4$ thin films were studied using UV–visible spectra in the range 300–1100 nm as shown in Fig. 5. The absorption spectra to provide a useful tool for the investigation of induced transition and insight in the optical band gaps are controlled which is due to the lattice constant order—disorder in structure [45]. A common way to extract the direct band gap energy (E_g) from optical absorption spectra is the Tauc relation as given below [46, 47]

$$\alpha = \frac{A(h\nu - E_g)^{n/2}}{h\nu}, \tag{5}$$

where α is the linear absorption coefficient, h is the Planck's constant (6.6260×10^{-34} J s), E_g is the optical band gap energy, ν is the photon energy, A is the proportionality constant and n is any values among of 1/2, 2, 3/2, and 3 corresponding to the direct, indirect, forbidden direct and forbidden indirect transitions, respectively. To determine the band gap energy plot of straight line portion $(\alpha h\nu)^2$ against photon energy ($h\nu$) were plotted as shown in Fig. 6. The direct electronic transition of electrons located in high energy states in the valency band replaces the lower energy states in the conduction band as that of the behavior in Brillouin zone [48]. Generally the energy band gap is affected by several factors such as crystallite size, thickness of thin films, lattice strain and impurity phase [49]. The valence bands and conduction bands splits into discrete electronic levels the density. Hence the energy band gap decreases with increasing crystallite size due to the spacing between these levels. "The decrease in band gap in the present case may be attributed to the increase in the crystallization of the films which establishes the quantum confinement effect" [50]. It causes decrease in energy band gap due to increase in localized states inside the energy band gap. The optical band gap value of Cr^{3+} substituted nickel ferrite thin films are found to vary from 2.37 to 2.98 eV presented in Table 2. The thickness of the Cr^{3+} substituted $NiFe_2O_4$ thin films were measured by a surface profiler. It is observed that,

the films thickness was in the order of nanometer dimension (206–283) in the tabulated Table 2.

3.3 Magnetic properties

The magnetic measurements of all films under investigation were done using VSM at room temperature in the range − 15 kOe to 15 kOe as shown in Fig. 7. The magnetic measurements such as coercivity (H_c), saturation magnetization (M_s), retentivity (M_r) and remanence ration (M_r/M_s) were obtained from hysteresis loops and presented in Table 3. The saturation magnetization for pure nickel ferrite film is obtain to be 234.12 emu/cc at room temperature and after Cr^{3+} substitution, the saturation magnetization decreases from 163.46 to 44.26 emu/cc with increasing Cr^{3+} concentration accordingly. The decrease in saturation magnetization values can be explained on the basis of fact that, the Cr^{3+} ions have strong tendency to occupy the tetrahedral [B] site and its non-magnetic nature. Thus, reduction in saturation magnetization is due to replacing of Fe^{3+} ($5\mu_B$) by non-magnetic Cr^{3+} ($3\mu_B$) at octahedral site [B] site and Ni^{2+} ($2\mu_B$) at tetrahedral (A) site [51]. From Table 3, it is clear that the saturation magnetization, coercivity and remanence ratio decreases with increases Cr^{3+} concentration in $NiFe_2O_4$ thin films. The coercivity depends on the surface of film, micro-strain, interparticle interaction. The coercivity decreased from 276.14 to 85.21 Oe with increases in Cr^{3+} concentration may be due to the decrease in anisotropy field which in turn decreases the domain wall energy. The value of coercivity decrease with increases Cr^{3+} content is relative to the soft ferromagnetic behavior for their high-frequency transformers application [52]. The composition of cations at tetrahedral site (A) and octahedral site [B] strongly influences the saturation magnetization in spinel cubic structure. When Cr^{3+} content is increased the paramagnetic Cr^{3+} ions tend to be occupied at octahedral site [B]. It means that decrease in magnetic ions in octahedral site [B] reduces the magnetic moment of that site. The Neel's sub lattice model introduces the B–B, A–A and A–B interactions. Out of them the A–B interaction is responsible for ferromagnetic ordering. The theoretical magnetic moment was calculated using the Neel's formula [53].

$$\eta_{B(cal)} = |M_B - M_A|, \tag{6}$$

where M_B and M_A are the magnetic moment of the octahedral [B] and the tetrahedral (A) site, respectively. The observed Bohr magnetons were calculated using the following relation [54].

$$\eta_{B(obs)} = \frac{M_w \times M_s}{\mu_B \times N_A}, \tag{7}$$

where M_s is the saturation magnetization, M_w is molecular weight of the each composition, N_A is Avogadro's number and μ_B is Bohr magneton. The magnetic moments per formula unit in Bohr magneton (μ_B) are presented in Table 3. The magnetic moment decreases with increase in Cr^{3+} content which is attributed to greater occupancy of Cr^{3+} at [B] sites. However, as the Cr^{3+} substitution increases the reduction in the hysteresis loop is observed as shown in Fig. 8. The anisotropy is related to the coercivity through Brown's formula [55].

$$H_c = \frac{2K}{\mu_B M_s}, \tag{8}$$

where μ_B is Bohr magneton and K is the anisotropy energy constant. The reduction of magneto crystalline anisotropy

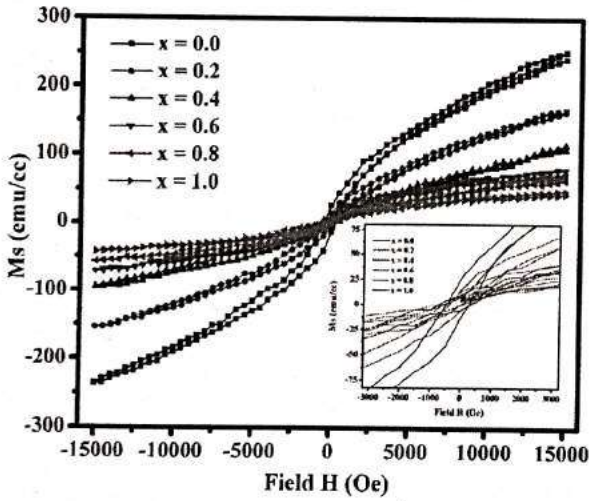

Fig. 7 Room temperature magnetization curve of $NiFe_{2-x}Cr_xO_4$ ($0.0 \le x \le 1.0$) thin films

Table 3 Saturation magnetization (M_s), remanence magnetization (M_r), coercivity (H_c), remanence ratio (R), Bohr's magneton number (μ_B) and anisotropy constant (K) of $NiFe_{2-x}Cr_xO_4$ ($0.0 \le x \le 1.0$) thin films

Composition x	M_s (emu/cc)	M_r (emu/cc)	H_c (Oe)	R	η_B (μ_B) (Obs)	η_B (μ_B) (Cal)	K (erg/cc)
0.0	234.12	26.98	267.14	0.1152	9.825	8.745	307,241
0.2	163.46	13.75	244.12	0.1841	5.202	1.561	103,789
0.4	111.53	12.42	233.54	0.1113	3.534	1.265	46,024
0.6	78.02	9.46	216.18	0.1215	2.461	0.548	20,754
0.8	65.12	7.44	206.46	0.1142	2.045	0.742	13,747
1.0	46.65	7.21	85.21	0.1545	1.459	0.456	2899

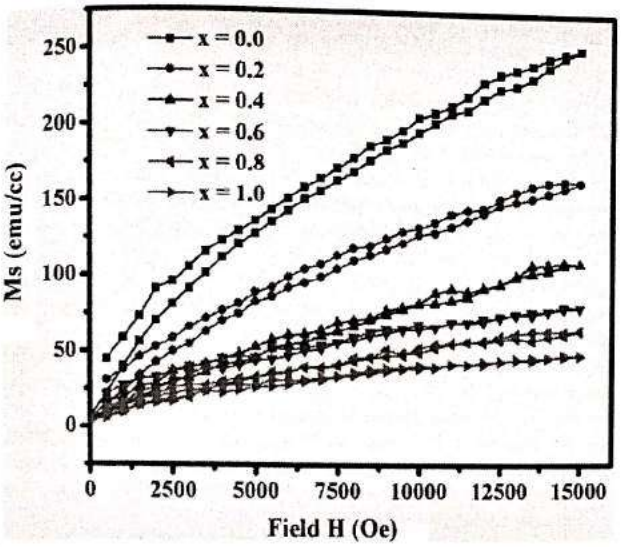

Fig. 8 M–H curves of Cr^{3+} substitution in $NiFe_2O_4$ ($0.0 \leq x \leq 1.0$)

energy is related to the decrease in coercivity [56]. The anisotropy constant decreases with the increasing of Cr^{3+} content, which leads to decrease in coercivity. The anisotropy constant of $NiFe_2O_4$ is due to a strong (s)–orbital (L) coupling in Ni^{2+} ions in the octahedral site. The Cr^{3+} ions is the zero angular momentum (1 = 0) which does not affected anisotropy constant. When Cr^{3+} ions were replaced with Fe^{3+} ions, the spin-orbital coupling weakened and anisotropy decreased [57, 58]. The change in anisotropy constant can be determined using the single ion anisotropy model which is due to positive value for the Fe^{3+} ions attributed to tetrahedral site (A) whereas negative value is attributed to the octahedral site [B].

4 Conclusion

The Cr^{3+} substituted $NiFe_2O_4$ thin films were successfully synthesized using spray pyrolysis technique. The XRD results shows that, the formation of single phase cubic structure of the thin film samples and the obeyed lattice constant were found to be 8.335–8.277 Å. FTIR spectra show two transmission bands around 442 and 655 cm^{-1} approving cubic structure. The optical absorption edges and band gap energy increases with increase in Cr^{3+} content. The Cr^{3+} substitution results in reduced saturation magnetization and also coercivity decreases, which is advantageous in high-frequency transformer application of thin films. The low anisotropy of the prepared thin films could not prevent a complete approach to saturation in these cases. From the results, the Cr^{3+} ions substitution in $NiFe_2O_4$ thin films were significantly changes in structural, optical and magnetic properties.

Acknowledgements The author Mr. Apparao R. Chavan is very much thankful to Solapur University, Solapur for providing XRD, Mysore University providing for AFM data and IIT madras providing for VSM facility.

References

1. K. Verma, A. Kumar, D. Varshney, Effect of Zn and Mg doping on structural, dielectric and magnetic properties of tetragonal $CuFe_2O_4$. Curr. Appl. Phys. **13**, 467–473 (2013)
2. E.R. Kumar, C. Srinivas, M. Seehra, M. Deepty, I. Pradeep, A. Kamzin et al., Particle size dependence of the magnetic, dielectric and gas sensing properties of Co substituted $NiFe_2O_4$ nanoparticles. Sens. Actuators A **279**, 10–16 (2018)
3. M. Ahamed, M.J. Akhtar, H.A. Alhadlaq, M.M. Khan, S.A. Alrokayan, Comparative cytotoxic response of nickel ferrite nanoparticles in human liver HepG2 and breast MFC-7 cancer cells. Chemosphere **135**, 278–288 (2015)
4. S.B. Kale, S.B. Somvanshi, M. Sarnaik, S. More, S. Shukla, K. Jadhav, Enhancement in surface area and magnetization of $CoFe_2O_4$ nanoparticles for targeted drug delivery application, in *AIP Conference Proceedings* (AIP Publishing, 2018), p. 030193
5. A.R. Chavan, M. Babrekar, A.C. Nawle, K. Jadhav, Impact of trivalent metal ion doping on structural, photoluminescence and electric properties of $NiFe_2O_4$ thin films. J. Electron. Mater. (2019). https://doi.org/10.1007/s11664-019-07329-w
6. P.B. Kharat, S.B. Somvanshi, J.S. Kounsalye, S.S. Deshmukh, P.P. Khirade, K. Jadhav, Temperature dependent viscosity of cobalt ferrite/ethylene glycol ferrofluids, in *AIP Conference Proceedings* (AIP Publishing, 2018), p. 050044
7. P.B. Kharat, S. More, S.B. Somvanshi, K. Jadhav, Exploration of thermoacoustics behavior of water based nickel ferrite nanofluids by ultrasonic velocity method. J. Mater. Sci. Mater. Electron. (2019). https://doi.org/10.1007/s10854-018-0386-1
8. M. Kokare, N.A. Jadhav, Y. Kumar, K. Jadhav, S. Rathod, Effect of Nd^{3+} doping on structural and magnetic properties of $Ni_{0.5}Co_{0.5}Fe_2O_4$ nanocrystalline ferrites synthesized by sol-gel auto combustion method. J. Alloys Compd. **748**, 1053–1061 (2018)
9. M. Gabal, A. Abdel-Daiem, Y. Al Angari, I. Ismail, Influence of Al-substitution on structural, electrical and magnetic properties of Mn–Zn ferrites nanopowders prepared via the sol–gel autocombustion method. Polyhedron **57**, 105–111 (2013)
10. D.K. Pradhan, S. Kumari, V.S. Puli, P.T. Das, D.K. Pradhan, A. Kumar et al., Correlation of dielectric, electrical and magnetic properties near the magnetic phase transition temperature of cobalt zinc ferrite. Phys. Chem. Chem. Phys. **19**, 210–218 (2017)
11. N. Jahan, A. Zakaria, Structural and electrical properties of chromium substituted nickel ferrite by conventional ceramic method. Mater. Sci. Pol. **34**, 185–191 (2016)
12. E.R. Kumar, R. Jayaprakash, S. Kumar, The role of annealing temperature and bio template (egg white) on the structural, morphological and magnetic properties of manganese substituted MFe_2O_4 (M = Zn, Cu, Ni, Co) nanoparticles. J. Magn. Magn. Mater. **351**, 70–75 (2014)
13. K. Omri, J. El Ghoul, O. Lemine, M. Bououdina, B. Zhang, L. El Mir, Magnetic and optical properties of manganese doped ZnO nanoparticles synthesized by sol–gel technique. Superlattices Microstruct. **60**, 139–147 (2013)
14. Y. Wang, L. Li, Y. Zhang, X. Chen, S. Fang, G. Li, Growth kinetics, cation occupancy, and magnetic properties of multimetal oxide nanoparticles: a case study on spinel $NiFe_2O_4$. J. Phys. Chem. C **121**, 19467–19477 (2017)

15. G.-L. Sun, J.-B. Li, J.-J. Sun, X.-Z. Yang, The influences of Zn^{2+} and some rare-earth ions on the magnetic properties of nickel–zinc ferrites. J. Magn. Magn. Mater. **281**, 173–177 (2004)
16. M. Ajmal, A. Maqsood, AC conductivity, density related and magnetic properties of $Ni_{1-x}Zn_xFe_2O_4$ ferrites with the variation of zinc concentration. Mater. Lett. **62**, 2077–2080 (2008)
17. R. Singh, J. Singh, B. Lal, M. Thomas, S. Bera, New $NiFe_{2-x}Cr_xO_4$ spinel films for O_2 evolution in alkaline solutions. Electrochim. Acta **51**, 5515–5523 (2006)
18. M. Raghasudha, D. Ravinder, P. Veerasomaiah, Influence of Cr^{3+} ion on the dielectric properties of nano crystalline Mg-ferrites synthesized by citrate-gel method. Mater. Sci. Appl. **4**, 432 (2013)
19. J. Lin, Y. He, X. Du, Q. Lin, H. Yang, H. Shen, Structural and magnetic studies of Cr^{3+} substituted nickel ferrite nanomaterials prepared by sol–gel auto-combustion. Crystals **8**, 384 (2018)
20. M. Shobana, H. Choe, Structural and electrical properties of Cr doped nickel ferrite. J. Mater. Sci. Mater. Electron. **27**, 13052–13056 (2016)
21. K. Panwar, S. Tiwari, K. Bapna, N. Heda, R. Choudhary, D. Phase et al., The effect of Cr substitution on the structural, electronic and magnetic properties of pulsed laser deposited $NiFe_2O_4$ thin films. J. Magn. Magn. Mater. **421**, 25–30 (2017)
22. E. Pervaiz, I. Gul, Low temperature synthesis and enhanced electrical properties by substitution of Al^{3+} and Cr^{3+} in Co–Ni nanoferrites. J. Magn. Magn. Mater. **343**, 194–202 (2013)
23. D. Beckel, A. Dubach, A.R. Studart, L.J. Gauckler, Spray pyrolysis of $La_{0.6}Sr_{0.4}Co_{0.2}Fe_{0.8}O_{3-\delta}$ thin film cathodes. J. Electroceram. **16**, 221–228 (2006)
24. K. Lethy, D. Beena, V. Mahadevan Pillai, V. Ganesan, Bandgap renormalization in titania modified nanostructured tungsten oxide thin films prepared by pulsed laser deposition technique for solar cell applications. J. Appl. Phys. **104**, 033515 (2008)
25. A.R. Chavan, R.R. Chilwar, P.B. Kharat, K. Jadhav, Effect of annealing temperature on structural, morphological, optical and magnetic properties of $NiFe_2O_4$ thin films. J. Supercond. Novel Magn. (2018). https://doi.org/10.1007/s10948-018-4565-3
26. A. Moholkar, G. Agawane, K.-U. Sim, Y. Kwon, K. Rajpure, J. Kim, Influence of deposition temperature on morphological, optical, electrical and opto-electrical properties of highly textured nano-crystalline spray deposited CdO: Ga thin films. Appl. Surf. Sci. **257**, 93–101 (2010)
27. A. Yadav, M. Barote, E. Masumdar, Studies on nanocrystalline cadmium sulphide (CdS) thin films deposited by spray pyrolysis. Solid State Sci. **12**, 1173–1177 (2010)
28. A. Takayama, M. Okuya, S. Kaneko, Spray pyrolysis deposition of NiZn ferrite thin films. Solid State Ion. **172**, 257–260 (2004)
29. A. Sutka, J. Zavickis, G. Mezinskis, D. Jakovlevs, J. Barloti, Ethanol monitoring by $ZnFe_2O_4$ thin film obtained by spray pyrolysis. Sens. Actuators B Chem. **176**, 330–334 (2013)
30. M. Babrekar, K. Jadhav, Synthesis and characterization of spray deposited lithium ferrite thin film. Int. Res. J. Sci. Eng. **Special Issue A1**, 73–76 (2017)
31. V. Sathyaseelan, P. Chandramohan, S. Velmurugan, High temperature dissolution of chromium substituted nickel ferrite in nitrilotriacetic acid medium. J. Nucl. Mater. **481**, 53–61 (2016)
32. S. Patange, S.E. Shirsath, B. Toksha, S.S. Jadhav, S. Shukla, K. Jadhav, Cation distribution by Rietveld, spectral and magnetic studies of chromium-substituted nickel ferrites. Appl. Phys. A **95**, 429–434 (2009)
33. P. Jadoun, J. Sharma, S. Kumar, S. Dolia, D. Bhatnagar, V. Saxena, Structural and magnetic behavior of nanocrystalline Cr doped Co–Mg ferrite. Ceram. Int. **44**, 6747–6753 (2018)
34. A. Costa, V. Silva, H. Ferreira, A. Costa, D.R. Cornejo, R. Kiminami et al., Structural and magnetic properties of chromium-doped ferrite nanopowders. J. Alloys Compd. **483**, 655–657 (2009)
35. A. Bagade, V. Ganbavle, K. Rajpure, Physicochemical properties of spray-deposited $CoFe_2O_4$ thin films. J. Mater. Eng. Perform. **23**, 2787–2794 (2014)
36. A. Raghavender, D. Pajic, K. Zadro, T. Milekovic, P.V. Rao, K. Jadhav et al., Synthesis and magnetic properties of $NiFe_{2-x}Al_xO_4$ nanoparticles. J. Magn. Magn. Mater. **316**, 1–7 (2007)
37. M. Lakshmi, K.V. Kumar, K. Thyagarajan, An investigation of structural and magnetic properties of Cr–Zn ferrite nanoparticles prepared by a sol–gel process. J. Nanostruct. Chem. **5**, 365–373 (2015)
38. B. Zhou, Y.-W. Zhang, C.-S. Liao, C.-H. Yan, Magnetism and phase transition for $CoFe_{2-x}Mn_xO_4$ nanocrystalline thin films and powders. J. Magn. Magn. Mater. **247**, 70–76 (2002)
39. F. Nesa, A. Zakaria, M.S. Khan, S. Yunus, A. Das, S.-G. Eriksson et al., Structural and magnetic properties of Cr^{3+} doped Mg ferrites. World J. Condens. Matter Phys. **2**, 27 (2012)
40. H. Kumar, J.P. Singh, R. Srivastava, P. Negi, H. Agrawal, K. Asokan, FTIR and electrical study of dysprosium doped cobalt ferrite nanoparticles. J. Nanosci. (2014). https://doi.org/10.1155/2014/862415
41. J.S. Kounsalye, A.V. Humbe, A.R. Chavan, K. Jadhav, Rietveld, cation distribution and elastic investigations of nanocrystalline $Li_{0.5+0.5x}Zr_xFe_{2.5-1.5x}O_4$ synthesized via sol–gel route. Physica B Condens. Matter **547**, 64–71 (2018)
42. M. Mozaffari, S. Manouchehri, M. Yousefi, J. Amighian, The effect of solution temperature on crystallite size and magnetic properties of Zn substituted Co ferrite nanoparticles. J. Magn. Magn. Mater. **322**, 383–388 (2010)
43. S. Mansour, M. Abdo, S. El-Dek, Improvement of physico-mechanical properties of Mg–Zn nanoferrites via Cr^{3+} doping. J. Magn. Magn. Mater. **422**, 105–111 (2017)
44. A.C. Nawle, A.V. Humbe, M. Babrekar, S. Deshmukh, K. Jadhav, Deposition, characterization, magnetic and optical properties of Zn doped $CuFe_2O_4$ thin films. J. Alloys Compd. **695**, 1573–1582 (2017)
45. K. Omri, O. Lemine, L. El Mir, Mn doped zinc silicate nanophosphor with bifunctionality of green-yellow emission and magnetic properties. Ceram. Int. **43**, 6585–6591 (2017)
46. K. Omri, N. Alonizan, Effects of ZnO/Mn concentration on the micro-structure and optical properties of ZnO/Mn–TiO_2 Nanocomposite for applications in photo-catalysis. J. Inorg. Organomet. Polym Mater. **29**, 203–212 (2019)
47. M.V. Khedkar, S.B. Somvanshi, A.V. Humbe, K. Jadhav, Surface modified sodium silicate based superhydrophobic silica aerogels prepared via ambient pressure drying process. J. Non-Cryst. Solids **511**, 140–146 (2019)
48. A.R. Chavan, S.D. Birajdar, R.R. Chilwar, K. Jadhav, Structural, morphological, optical, magnetic and electrical properties of Al^{3+} substituted nickel ferrite thin films. J. Alloys Compd. **735**, 2287–2297 (2018)
49. C. Lokhande, E.-H. Lee, K.-D. Jung, O.-S. Joo, Ammonia-free chemical bath method for deposition of microcrystalline cadmium selenide films. Mater. Chem. Phys. **91**, 200–204 (2005)
50. J.J. Vijaya, G. Sekaran, M. Bououdina, Effect of Cu^{2+} doping on structural, morphological, optical and magnetic properties of $MnFe_2O_4$ particles/sheets/flakes-like nanostructures. Ceram. Int. **41**, 15–26 (2015)
51. Y. Köseoğlu, M.I.O. Olciwi, R. Yilgin, A.N. Koçbay, Effect of chromium addition on the structural, morphological and magnetic properties of nano-crystalline cobalt ferrite system. Ceram. Int. **38**, 6671–6676 (2012)
52. Y. Köseoğlu, Structural and magnetic properties of Cr doped NiZn-ferrite nanoparticles prepared by surfactant assisted hydrothermal technique. Ceram. Int. **41**, 6417–6423 (2015)
53. P.B. Kharat, A.R. Chavan, A.V. Humbe, K. Jadhav, Evaluation of thermoacoustics parameters of $CoFe_2O_4$–ethylene glycol

nanofluid using ultrasonic velocity technique. J. Mater. Sci. Mater. Electron. **30**, 1175–1186 (2019)
54. A.R. Chavan, J.S. Kounsalye, R.R. Chilwar, S.B. Kale, K. Jadhav, Cu^{2+} substituted $NiFe_2O_4$ thin films via spray pyrolysis technique and their high-frequency devices application. J. Alloys Compd. **769**, 1132–1145 (2018)
55. S.E. Shirsath, B. Toksha, R. Kadam, S. Patange, D. Mane, G.S. Jangam et al., Doping effect of Mn^{2+} on the magnetic behavior in Ni–Zn ferrite nanoparticles prepared by sol–gel auto-combustion. J. Phys. Chem. Solids **71**, 1669–1675 (2010)
56. R.R. Chilwar, A.R. Chavan, M. Babrekar, K. Jadhav, Impact of trivalent metal ion substitution on structural, optical, magnetic and dielectric properties of $Li_{0.5}Fe_{2.5}O_4$ thin films. Physica B Condens. Matter **566**, 43–49 (2019)
57. L. Kumar, P. Kumar, M. Kar, Influence of Mn substitution on crystal structure and magnetocrystalline anisotropy of nanocrystalline $Co_{1-x}Mn_xFe_{2-2x}Mn_{2x}O_4$. Appl. Nanosci. **3**, 75–82 (2013)
58. L. Kumar, M. Kar, Influence of Al^{3+} ion concentration on the crystal structure and magnetic anisotropy of nanocrystalline spinel cobalt ferrite. J. Magn. Magn. Mater. **323**, 2042–2048 (2011)